Quasielastic scattering of ^{6}He on ^{9}Be at 25 MeV/nucleon

Y. L. Ye,[1,*] D. Y. Pang,[1] D. X. Jiang,[1] T. Zheng,[1] Q. J. Wang,[1] Z. H. Li,[1] X. Q. Li,[1] Y. C. Ge,[1] C. Wu,[1] G. L. Zhang,[1] Q. Y. Hu,[1] J. Wang,[1] Z. Q. Chen,[1] A. Ozawa,[2,†] Y. Yamaguchi,[2] R. Kanungo,[2] and I. Tanihata[2,‡]

[1]*School of Physics and MOE Key Laboratory of Heavy Ion Physics, Peking University, Beijing, China*

[2]*RIKEN, 2-1 Hirosawa, Wako, Saitama 351-0198, Japan*

(Received 14 August 2004; published 13 January 2005)

Differential cross sections for the quasielastic scattering of a 25 MeV/nucleon ^{6}He on a ^{9}Be target have been measured. A double-folding model approach has been applied to generate the real part of the optical potential. An optical model analysis has been carried out to study the potential parameters by optimally fitting the experimental angular distribution. In the context of the coupled-channel calculation the contribution of the inelastic channels to the experimental data has been found to be small. The effect of the unstable property of the ^{6}He nucleus is discussed.

DOI: 10.1103/PhysRevC.71.014604 PACS number(s): 25.60.Bx, 25.70.Bc, 24.10.Ht

I. INTRODUCTION

Elastic scattering has long been studied to explore the effective interaction, known as the optical potential (OP), between colliding nuclei [1]. In addition to being important in itself, this potential is also necessary for describing the entrance and exit channel potentials for more complicated reaction processes such as fusion, breakup, and few-nucleon transfer [2,3]. Since the discovery of halo nuclei [4] the study of nuclear structure and reactions for unstable nuclei has generated considerable worldwide interest [5]. Experiments were first carried out to measure the interaction cross sections and momentum distributions of the fragments generated by the breakup of unstable projectiles [6]. In recent years elastic scattering has also been measured for some unstable nuclei [7]. In relation to the lightest halo nucleus ^{6}He, elastic scattering has been measured for proton targets at RIKEN (73 *A* MeV [8]), GANIL (41.6 *A* MeV [9] and 38.3 *A* MeV [10]), Dubna (25 *A* MeV [11]), and GSI (about 700 *A* MeV [12]) by applying the method of inverse kinematics. In general, these data can be well described in the context of the folding-model approach. The data relevant to ^{6}He scattering from complex targets are still very scarce and their theoretical interpretations are more complicated. So far, only the measurements for a ^{4}He target at a few relatively low energies [13] and for a ^{12}C target at 38.3 MeV/nucleon [6] have been reported for limited angular ranges. The relevant theoretical analysis has revealed interesting coupling effects related to the weakly bound property of the halo nucleus.

Herein we report the measurement of quasielastic scattering of $^{6}\mathrm{He} + {}^{9}\mathrm{Be}$ at 25 MeV/nucleon in the laboratory system (lab). The purpose of this paper is to obtain the optical potential for this colliding system and to provide the basis for a further study of the breakup and neutron-transfer reactions that have also been measured in the present experiment and will be reported later.

II. EXPERIMENTAL DETAILS

The experiment was carried out at RIKEN in Japan with the RIKEN Projectile Fragment Separator (RIPS) radioactive ion beam line [14]. The schematic diagram of the experimental setup is shown in Fig. 1. The secondary beam was produced by the fragmentation of a 70 MeV/nucleon ^{13}C primary beam on a thick (8 mm) ^{9}Be target. The ^{6}He ions at 25 MeV/nucleon were separated by the RIPS beam line equipped with two dipole magnets D1 and D2, and a set of beam-monitoring detectors were placed around the focal points F1 and F2. The beam was then transported to the experimental area around the focal point F3. The contamination of the ^{6}He beam was reduced to less than 10% by applying an aluminum wedge degrader at F1. This contamination can be eliminated through offline analysis by applying cuts on the time of flight (TOF) between the plastic scintillation counters at F2 (F2-Plastic) and F3 (F3-Plastic) or, alternatively, between F2-plastic and F3-PPAC2 if F3-Plastic was removed, and on the energy loss (ΔE) of the ions in the plastic scintillation counters. A ^{9}Be foil with an effective size of 40×30 mm^2 and a thickness of 100 μm was used as the physics target. The target was tilted at an angle of 45° with respect to the beam direction to allow for adequate space for the appropriate detector setup. The outgoing particles were detected by an array of six telescopes (T1–T6). Each telescope consists of a position-sensitive silicon detector (PSD) [15], which has a position resolution of about 2.5 mm full width at half maximum (FWHM) in either the *X* or the *Y* dimension, a large surface silicon detector (SSD), and a CsI(Tl) scintillation detector. Each PSD or SSD has a thickness of 325 μm and a sensitive area of 45×45 mm^2. The CsI(Tl) crystal has a front surface of 50×50 mm^2 and was shaped to a smaller size at the rear surface to match the surface of a photodiode with an effective area of 18×10 mm^2. The energy resolutions of the PSD, SSD, and CsI(Tl) are about 2%, 0.5%, and 8.6%, respectively, and have been tested by an ^{241}Am α source.

*Corresponding author: yeyl@pku.edu.cn.

†Present address: Institute of Physics, University of Tsukuba, Tsukuba, Ibaraki 305-8571, Japan.

‡Present address: Argonne National Laboratory, 9700 South Cass Avenue, Argonne, IL 60439.

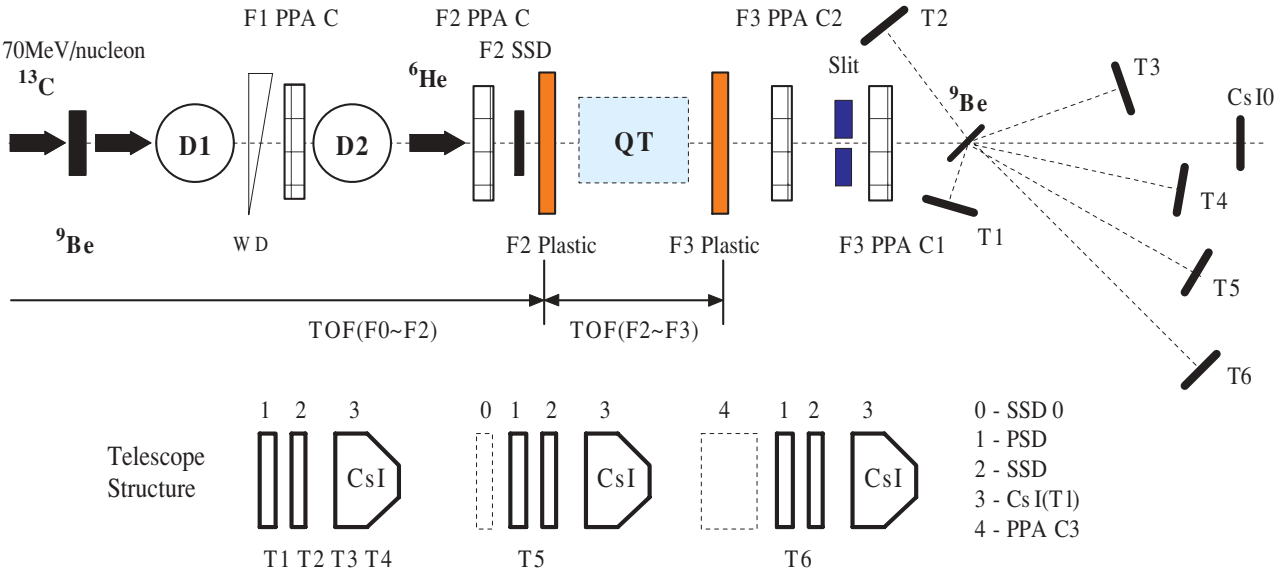

FIG. 1. (Color online) Schematic view of the experimental setup.

The setup shown in Fig. 1 has been basically designed for transfer reaction, but the elastic scattering data can be recorded simultaneously. Since the data at small angles are of special importance in determining the surface part of the OP, we have taken some low beam intensity (of about 5×10^3 pps) runs with the telescope T2 moving to 0° (0°-T2) and at a distance of 218.5 mm downstream from the target. In this case the F3-Plastic was removed to avoid the production of significant background scattering events that could go directly into 0°-T2. Two parallel-plate avalanche counters (PPAC1 and PPAC2 at F3) [16] were mounted upstream from the target to monitor the incident particles. Each PPAC measures both the *X* and *Y* positions of the traveling particles with an uncertainty of less than 1 mm in either dimension. In addition, each PPAC provides a fast timing signal from its anode plane.

In general, the beam-monitoring detectors must be thin. This should be, especially, the case for those detectors close to the target. These thin detectors may not be able to collect enough energy loss from the traveling particles to build the particle identification spectrum with sufficient quality. To ensure accurate knowledge of the beam compositions, including all kinds of small contaminations, we removed the target and used the 0°-T2 to do a detailed analysis. Figure 2(a) shows the original situation with no selection on the incident beam and Table I shows the quantitative results of the beam ingredients, namely, 89.8% ^{6}He, 4% ^{9}Be, and smaller percentages of few others. The tails around the ^{6}He peak have been generated by the scrape of the incident particles at the target frame (ig08, 1.6%), by the reaction in the thick CsI detector material (ig07, 2.1%), by the tunneling effect in the Si detector (ig10, 2.0%), and by the electronic signal pileup (ig09, 0.19%) caused by the very large counting rate for 0° detection. It can be seen that the contaminations and the tails represent only very small portions of the total number of incident particles. We, subsequently, applied a cut on the TOF detected by the upstream beam monitors and a cut on the beam spot at the target position (±5 mm in both the *X* and *Y* directions), which is a beam cross section projected from PPAC1 and PPAC2 positions. The resulting beam contents are shown in Fig. 2(b). The contaminations from isotopes other than ^{6}He have been totally removed except for a very small portion of tritons (less than 0.1%), which have no influence on the ^{6}He elastic data. The tail generated by the scrape at the target frame almost disappears since the beam spot was limited to be smaller than the target frame. The other three tails around the ^{6}He peak still exist but amount to less than 4.5% of the total counts. We consider these tail events to be good ^{6}He events since they were only shifted outside of the peak by their detection after reaction with the target.

Data analysis for the 0° telescope is a delicate task [17]. First we need to define a straight line (*Z* axis) for the whole detection system. The direct measurement using a laser beam often introduces an uncertainty of millimeters because of the inevitable mounting and dismounting of detectors along the beam line. We have, therefore, adopted a method relying on online detection by the position-sensitive detectors when the

TABLE I. Ingredient of the beam.

Number	Ingredient	Percentage
ig01	^{6}He	89.8
ig02	^{9}Be	4.0
ig03	^{7}Li	0.11
ig04	^{8}Li	0.041
ig05	^{3}H	0.11
ig06	^{4}He	0.028
ig07	reaction in detectors	2.1
ig08	scatter from target frame	1.6
ig09	pile up	0.19
ig10	tunneling	2.0

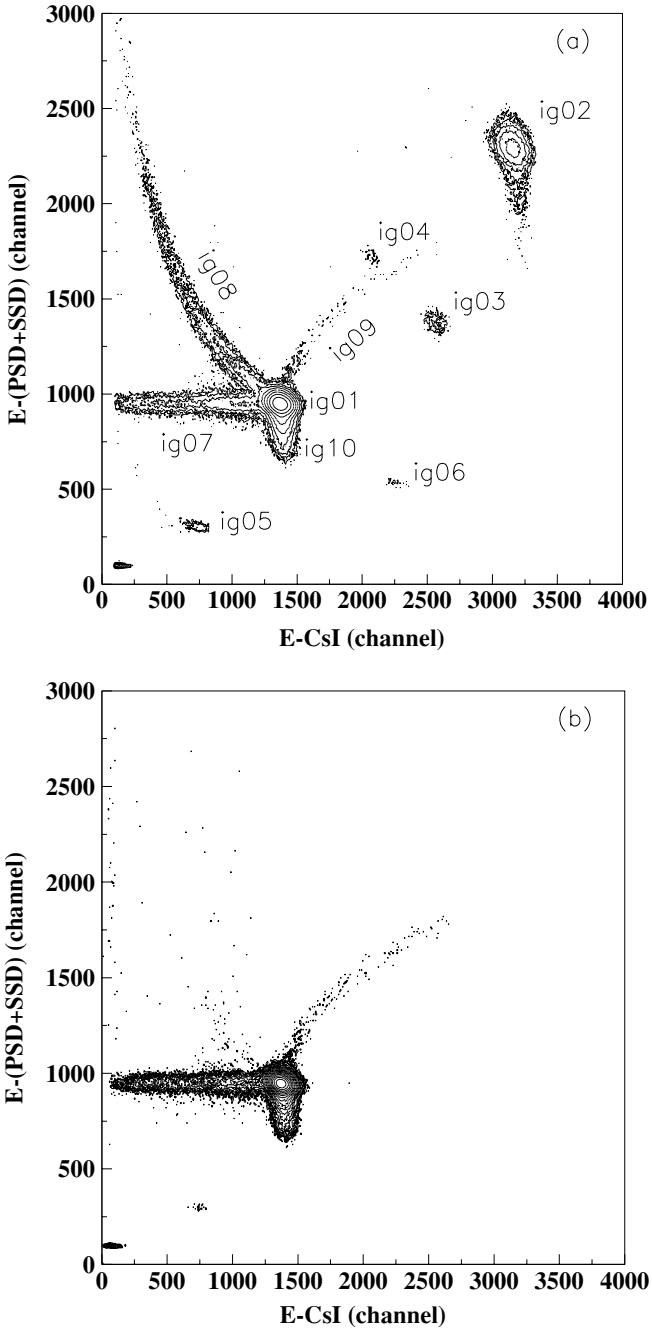

FIG. 2. The composition of the incident beam. (a) Original beam; and (b) beam subject to a cut on the TOF detected by the upstream beam monitors and a cut on the beam spot at the target position (see the text for details). The energies are plotted with arbitrary units.

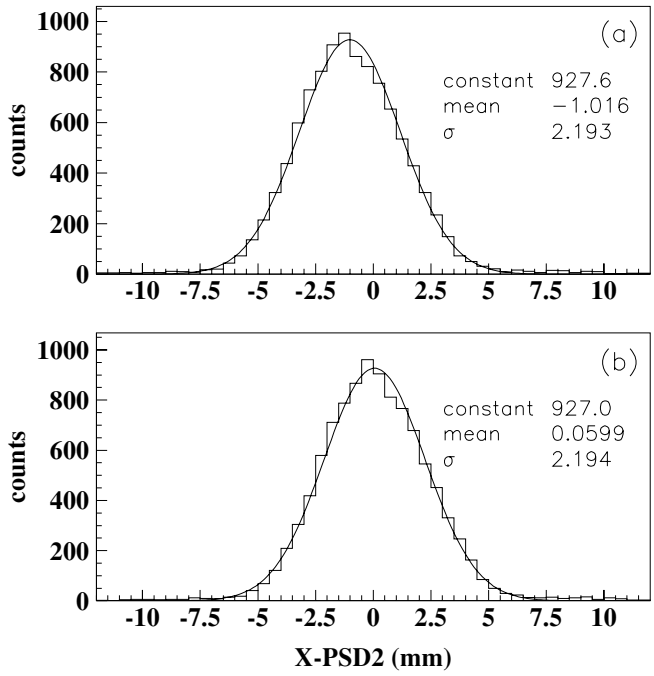

FIG. 3. Beam profile at X dimension measured by the PSD of 0°-T2 before (a) and after (b) the adjustment of the offset.

target was moved out (target-out). The real beam profiles were used to adjust the offsets of the position distributions measured by PPAC1, PPAC2, and 0°-T2 so that the centers of the profiles all match a straight line (Z axis). Figure 3 depicts an example of the profile measured by the PSD of 0°-T2 before (a) and after (b) the adjustment of the offset. To get a higher accuracy only the central part of the beam, selected by PPAC1 and PPAC2, was used to define this offset for the PSD of 0°-T2. As a result of such an approach the absolute uncertainty of the Z axis (beam direction) is less than 0.1°. The precise definition of this 0° axis is necessary since the elastic scattering cross sections vary rapidly at small angles and a small angular deviation may result in a significant error in the measurement of the cross-section value.

The positions at PPAC1 and PPAC2 were determined by a time-difference method prior to which the calibration had been carried out [16]. For the PSDs the positions are determined by a charge-division method prior to which the calibration had been performed only through the use of a radioactive source [15]. We checked the calibration through the use of the actual beam by comparing the positions measured by the PSD with those projected from the PPAC1 and PPAC2, for target-out runs. Consistent calibration factors were obtained. They confirm the applicability of the PSD at various energies and counting rates. The scattering angles could then be calculated event by event. Figure 4 shows the experimental angular distributions of the elastically scattered ^{6}He particles for target-in (solid line) and target-out (dotted line) runs, which were normalized to have the same number of incident particles. A selection of the good incident beam particles was determined by applying cuts on the TOF and on the beam spot at the target position. The cuts were the same as those used for Fig. 2(b). The difference between the target-in and target-out spectra is very small owing to the small scattering probability. The inset picture in Fig. 4 gives an idea of the effect of the target, which reduces the number of outgoing particles at very small angles ($\theta_{\rm lab}$ smaller than about 0.6°) but increases the scattered events at larger angles. The differential cross sections could then be extracted by subtracting the target-out spectrum from the target-in spectrum. By requiring that the difference of the counts for target-in and target-out runs in the same angular slice be three

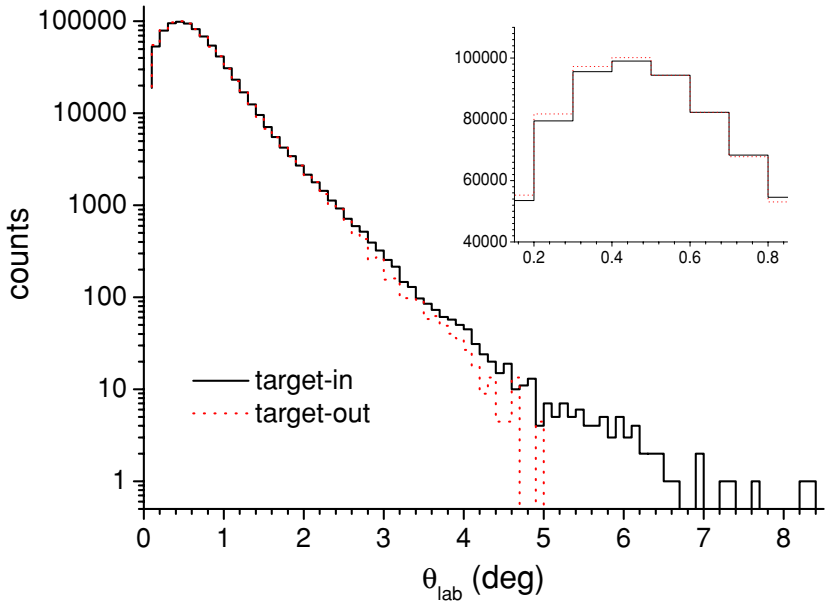

FIG. 4. (Color online) Angular distribution of the ^{6}He particles for target-in (solid line) and target-out (dotted line) runs, detected by the 0° telescope. The inset is a linear display of the counts at very small angles.

times larger than the square root of the target-out counts, a value that corresponds to a statistical significance of larger than 99%, we were able to obtain the elastic scattering differential cross sections starting from a 1.5° lab angle.

The angular resolution of the whole detection system can also be analyzed using the data of the target-out events. We define a "pencil beam" by requiring a beam size to be less than 1 mm at the centers of both PPAC1 and PPAC2. Then the spot size measured by the 0°-T2 gives approximately the overall position resolution related to the performances of PPAC1, PPAC2, and the PSD of 0°-T2. This resolution was determined to be about 2.4 mm (FWHM), which is consistent with the prior calibration using a radioactive source and corresponds to an overall angular resolution of about 0.7°(FWHM) in the lab system. Taking this angular uncertainty into consideration we built the data points for every 1.5° slice. The solid angle for each data point was calculated by the Monte Carlo simulation method taking into account the real incident angular distribution of the beam particles and the geometry of the detector setup. Finally, the differential cross sections recorded by 0°-T2 and presented as the ratio to the Rutherford cross sections were plotted in Fig. 7 as the first five points up to 12.5° in the center of mass (c.m.) system.

To extend the data to larger angles, the 0°-T2 was moved away and the beam intensity was increased to the highest available value of about 2×10^5 pps. The elastic scattering data were recorded by T4, T3, and T5 together with the breakup and transfer data. Figure 5 depicts an example of the particle-identification picture obtained by T4. It is obvious that the isotopes with $Z = 1$ through $Z = 4$ are clearly identified.

One problem encountered during the experiment was that the high beam intensity exceeded the rate capability of the cathode planes of the upstream PPACs. As a result, the latter failed to track the incident particles, but they still provided good timing signals that can be used to monitor the number of incident particles. To limit the beam spot on the target, we placed a collimation slit of 20×20 mm^2 between the PPAC2 and the PPAC1, as is seen in Fig. 1. The relatively large slit allowed for a large acceptance of the incident particles (about 80%) but degraded the angular resolution of the detection system to 4°–6° in the lab system, depending on the distances between the telescopes and the target. Consequently, we only divided the PSDs of T4 and T3 into three and two angular slices, respectively; because of extremely low counts T5 was not divided at all.

Figure 6 depicts an example of the energy spectrum of the ^{6}He detected by T4 with the target-out background subtracted. In this spectrum a high-energy peak can be clearly identified. This peak corresponds to quasielastic scattering. The

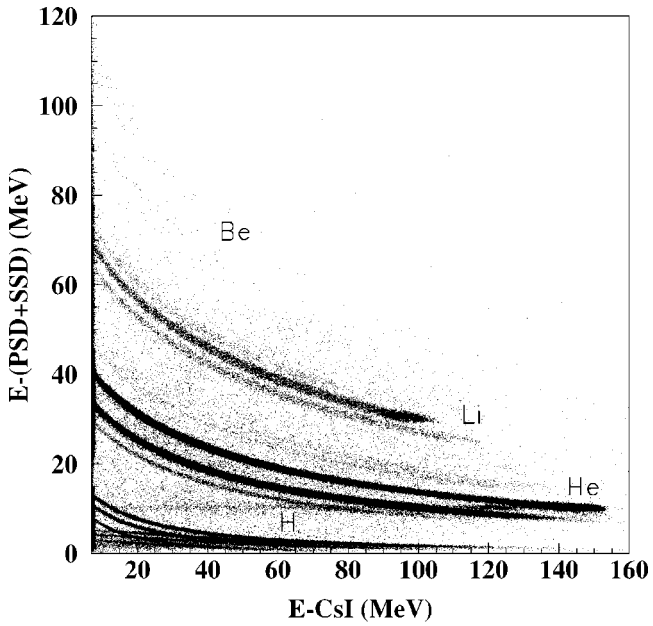

FIG. 5. Particle identification achieved by telescope T4, plotted as energy loss in PSD+SSD vs energy loss in CsI.

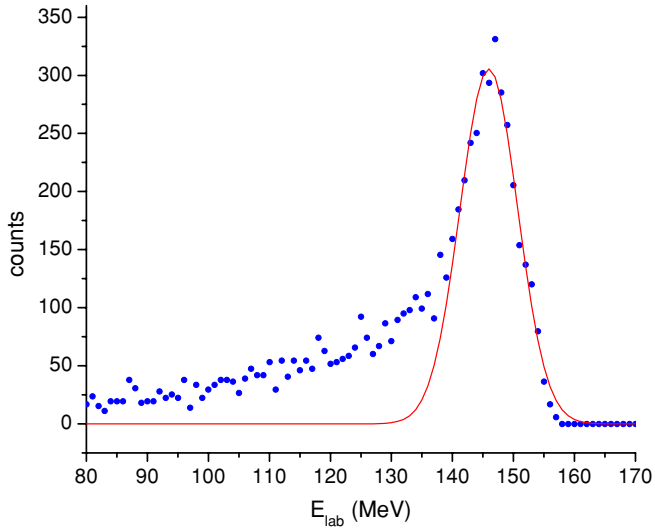

FIG. 6. (Color online) Energy distribution of ^{6}He isotopes detected by T4 (dots) and a fit of the high-energy peak with a function of the Gaussian form (solid line).

low-energy tail coming from complex processes may introduce a systematic error of about 10% when determining the peak counts by a Gaussian function fit. Again, the solid angle of each part of the telescopes was calculated by a Monte Carlo method similar to that for 0°-T2. The number of incident particles was recorded by the anode plane of PPAC2. Its efficiency and background rate was cross-checked by taking coincidences with other detectors. The fraction of accepted ^{6}He within the total number of incident particles was determined by applying a cut on the TOF. The final results are presented in Fig. 7 for the c.m. angles between 13° and 50°. The error bars in the figure are statistical only, resulting from the target-in count numbers and the corresponding background subtractions. In addition, a systematic error of about 15% should be considered, on account of the uncertainties in determining the quasielastic peak in the energy spectrum, the solid angle, and the number of incident ^{6}He ions.

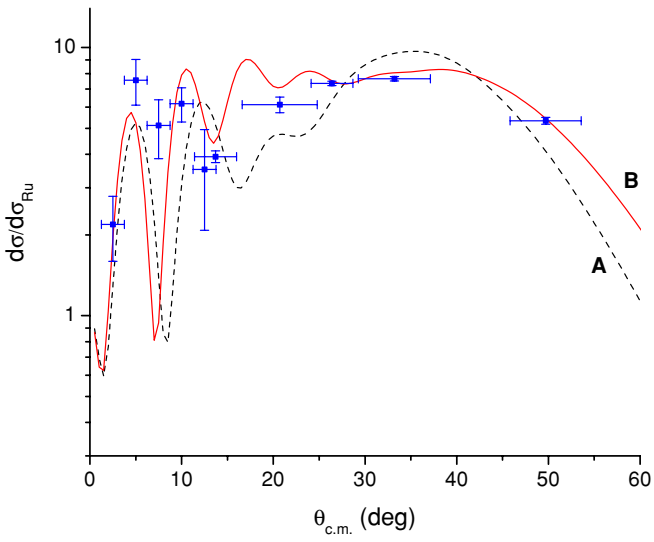

FIG. 7. (Color online) Differential cross sections of the elastic scattering of a 25 MeV/nucleon ^{6}He from a ^{9}Be target. The solid points represent the experimental data, the dashed line corresponds to the optical model calculation with parameter set A in Table II, and the solid line corresponds with parameter set B.

III. ANALYSIS AND DISCUSSION

The measurement of elastic scattering through the use of silicon detector telescopes [17,18] suffers from relatively large angular uncertainty when compared to the measurement obtained through the use of a magnetic spectrometer [6]. The method proposed here, however, may have certain advantages in rendering the measurement possible at very small as well as relatively large angles. In our case (Fig. 7) the fine oscillation structure at small angles has been averaged out owing to the large horizontal error bars, but the period of change can still be identified. The cross sections at small angles reveal a significant enhancement over the Rutherford cross sections. This phenomenon has also been observed in the scattering of ^{11}Li [18] and ^{6}He [6] from ^{12}C targets and has been attributed to the enhanced refractive effect at the far surface of the halo nucleus. The enhancement is even more significant in the present experiment, probably because, in addition to the unstable property of the projectile, the extended nuclear matter distribution of the ^{9}Be target (as will be described in what follows) may also contribute. It should be noted that, owing to the large nonlinearity at very small angles, the Rutherford cross sections used in the ratio presentation have been averaged over the angular range that corresponds to the horizontal error bars in the figure. One way of avoiding this complication is to evaluate the absolute cross sections instead of the ratio, but this would not make a meaningful difference when compared to the theoretical calculations.

A. Folding model potential

It is well known that the double-folding model with effective nucleon-nucleon (*NN*) interactions and realistic nuclear matter density distributions could be used to generate the real part of the OP for scattering between stable nuclei [1]. For unstable nuclei the strong breakup effect at the surface reduces the real potential and increases the absorption. This could be accounted for by the change of the OP parameters or by an augmentation of the so-called dynamic polarization potential (DPP) [6]. We also take the folded potential as a starting point to search for the OP parameters.

The double-folding model has been described in Ref. [1,19]; the real part of the OP is given in the form

$$V_F = \int d\mathbf{r}_2 \int d\mathbf{r}_1 \rho_1(\mathbf{r}_1)\rho_2(\mathbf{r}_2)v(\mathbf{R}-\mathbf{r}_1+\mathbf{r}_2), \qquad (1)$$

where $\rho_1(\mathbf{r}_1)$ and $\rho_2(\mathbf{r}_2)$ are the density distributions of the projectile and the target, respectively, and v is the effective *NN* interaction. The latter is chosen as the usual M3Y form based on the *G*-matrix elements of the Paris *NN* interaction,

including a knock-on exchange term:

$$v_{\rm pt}(r) = \left[11062\frac{e^{-4r}}{4r} - 2538\frac{e^{-2.5r}}{2.5r}\right] - 590\left[1 - 0.002\frac{E}{A}\right]\delta(r), \quad (2)$$

where E/A is the bombarding energy per nucleon in MeV. We use the code DFPOT [20] to perform the calculation. The nuclear matter density distribution for ^{9}Be was described in Ref. [21] as

$$\rho(r) = (A + BC^2r^2)e^{-C^2r^2} + (D + EF^2r^2)e^{-F^2r^2}, \quad (3)$$

with $A = 0.0651$, $B = 0.0398$, $C = 0.5580$, $D = 0.0544$, $E = 0.0332$, and $F = 0.4878$. This distribution gives a large root-mean-square (rms) radius of 2.73 fm. For ^{6}He the "realistic" density distribution, taking into account the large spatial distribution of the valence neutrons, was adopted [22]:

$$\rho_i(r) = N_{ci}\frac{e^{-r^2/a^2}}{\pi^{3/2}a^3} + N_{vi}\frac{2e^{-r^2/b^2}}{3\pi^{3/2}b^5} \times \left[Ar^2 + B\left(r^2 - \frac{3b^2}{2}\right)^2\right] (\mathrm{i} = n,\ p), \quad (4)$$

with $N_{cn} = 2$, $N_{cp} = 2$, $N_{vn} = 2$, $N_{vp} = 0$, $a = 1.55$ fm, $b = 2.24$ fm, $A = 1$, and $B = 0$. The rms radius of this distribution is 2.57 fm, which is consistent with the experimental value [4,23]. We have compared this distribution with the Gaussian distribution used in Ref. [6] and found almost no difference.

Various density- and energy-dependent effective *NN* interactions have been developed [1,6]. When used in the double-folding model, these interactions give quite different depths of the real potentials while effecting only small changes of the radius and diffusiveness. Since the depth will be adjusted in the optical model (OM) analysis, we have decided to use simply the original M3Y-Paris *NN* interaction as described in the foregoing, neglecting the density-dependent term. Also, to maintain flexibility in adjusting all the parameters the folded potential was fit by a function of the standard Wood-Saxon (WS) form:

$$V(r) = \frac{V}{1 - \exp\left(\frac{r - R_v}{a_v}\right)}. \quad (5)$$

The parameters obtained are $V = 130.5$ MeV, $R_v = 2.52$ fm, and $a_v = 1.05$ fm for the depth, radius, and diffusesiveness, respectively.

B. Optical model analysis

In performing the OM calculations the code ECIS97 [24] was used. The OP has been expressed by a sum of three terms:

$$U(r) = V(r) + iW(r) + V_C(r), \quad (6)$$

where $V(r)$ is the real potential of WS form with its parameters initially provided by a folding model calculation, $W(r)$ is the phenomenological imaginary potential of the WS form with W, R_w, and a_w as its depth, radius, and diffusesiveness respectively, and $V_C(r)$ is the Coulomb potential corresponding to an uniformly distributed charge sphere of radius $R_c = r_c(A_p^{1/3} + A_t^{1/3})$ with $r_c = 1.2$ fm. To compare with the results of the other colliding systems, the reduced radii r_w and r_v were defined as $r_i = R_i/(A_p^{1/3} + A_t^{1/3})(i = v, w)$, where A_p and A_t are the mass numbers of the projectile and the target, respectively. Since the angular resolution of our measurement is poor we neglect the spin-orbit potential, which is only useful for improving the description of some fine structure of the angular distribution. The imaginary part of the OP was studied systematically in Ref. [6] for a ^{12}C target bombarded by various light projectiles including ^{6}He. It was found that the reduced radius $r_w = 0.97$ fm is appropriate for the light colliding systems at tens of MeV per nucleon. We also adopt this value and then search the parameters V, W, and a_w by optimal fit to the experimental data. The resulting parameters are presented as set A in Table II and the corresponding angular distribution is drawn as the dashed line in Fig. 7. Here a relatively large a_w may be attributed to the halo property of ^{6}He. It turns out that the depth of the real OP changes very little relative to its initial value. We note that this parameter set has a strong microscopic base as a result of the application of the double-folding model. In fact, if we fix the depth of the real potential as the value produced by the folding-model calculation ($V = 130.5$) and adjust the parameters of the imaginary potential, the results obtained are almost the same as presented by set A in Table II and the corresponding distribution of the cross section is indistinguishable from the dashed line in Fig. 7.

It can be seen that the angular distribution calculated with the OP parameter set A is somewhat out of phase in comparison to the data of the first two oscillations. This situation cannot be improved without changing the radius of the real potential. When we then released the r_v as an adjustable parameter the optimal fit would result in a r_v close to 1.0 fm. For simplicity we fix it to be 0.97 fm, the same as r_w. The parameters obtained are presented by set B in Table II. The corresponding angular distribution (solid line in Fig. 7) reproduces the structure of the experimental cross sections much better. The relatively large radius for the real potential was also observed in elastic scattering of other halo nuclei, such as ^{14}Be [17], which indicates an extended refractive effect at the surface of the halo nuclei.

It should be noted that the calculation significantly underestimated the second and third data points at around the maximum of the first oscillation. A similar discrepancy was already observed in an early experiment measuring elastic scattering of ^{11}Li from a ^{12}C target [18]. It was originally attributed to the contamination of the breakup events, but experimental and theoretical evidence in support of such a speculation has not been found so far [25]. We have checked

TABLE II. Optical potential parameters for ^{6}He + ^{9}Be at 25 MeV/nucleon.

Sets	V (MeV)	r_v (fm)	a_v (fm)	W (MeV)	r_w (fm)	a_w (fm)	σ_r (mb)
A	133.1	0.646	1.05	19.7	0.97	1.31	1663.4
B	114.8	0.97	1.05	36.4	0.97	1.27	2061.4
C	114.8	0.97	1.05	37.0	0.97	1.27	2102.9

the particle identification for various angles detected by 0°-T2 but could not find breakup α particles beside the ^{6}He peak. In addition, the importance of the breakup channel relative to the elastic channel can be evaluated quantitatively by using the telescopes T3, T4, and T5, which give a clear separation of the various helium isotopes. It is evident that the breakup channel becomes less important as the emitting angle decreases. The contamination of the breakup events should be negligible at least for angles below 8° (c.m.). Hence, the problem of this small-angle discrepancy has yet to be solved.

The OM analysis also results in the reaction cross sections shown in Table II. The values obtained here are relatively large probably due to the large halo extension of ^{6}He as well as the large radius of ^{9}Be, as previously described. To ascertain whether these values were reasonable we made a simple calculation by applying the Kox formula [17,26]. Taking the realistic radii of ^{6}He and ^{9}Be as the rms radii given by the density distributions in our double-folding calculations (i.e., 2.57 fm and 2.73 fm, respectively) we obtained a reaction cross section of 1592 mb. This value is quite close to the one deduced from our OP parameter set A. If the so-called neutron-excess terms [17] had been applied to both the projectile and the target the calculated reaction cross section could have been further increased by a few hundred millibarns. Of course, for the exotic nuclei the Kox formula may just provide a rough estimation. It will be interesting to carry out direct measurements of the reaction cross sections for double isospin-asymmetric systems, such as ^{6}He + ^{9}Be, at intermediate energies.

C. Effect of inelastic scattering

As already mentioned, the telescopes used in the present experiment did not provide enough energy resolution to separate the elastic and inelastic channels in the energy spectrum (Fig. 6). It is, consequently, important to evaluate the influence of inelastic scattering on the OP parameters, which, in principle, should only be determined by the elastic data. Since excited states of the projectile ^{6}He are not bound they do not contribute to the measurement. In contrast the target ^{9}Be is a p-shell odd-neutron nucleus with a relatively large deformation and rich excited states (Ref. [27] and references therein). In the context of the interaction with a spin-0 nucleus, such as α or ^{6}He, the major excitation of the ^{9}Be goes along the rotational band headed by the $3/2^-$ ground state. Therefore, we only need to consider the $5/2^-$ state at an excitation energy of 2.43 MeV and the $7/2^-$ state at 6.76 MeV [27]. Again, we used the code ECIS97 to pursue the coupled-channel calculation in the framework of the symmetric rotational model where the quadruple deformation parameter β_2 plays an important role. For ^{9}Be, β_2 may range from 0.52 to 1.3 as reported in the literature. However, a direct measurement of the inelastic scattering combined with theoretical analysis cited in [27] for the system α + ^{9}Be at 65 MeV should provide a more reliable context for our analysis. The value of β_2 for ^{9}Be obtained through the analysis in [27] ranges between 0.52 and 0.66. For simplicity, we use its mean value, that is, 0.59.

Having started from the OP parameter set B (Table II) we compared the sum of the calculated elastic and inelastic cross sections with the experimental data. The comparison reveals

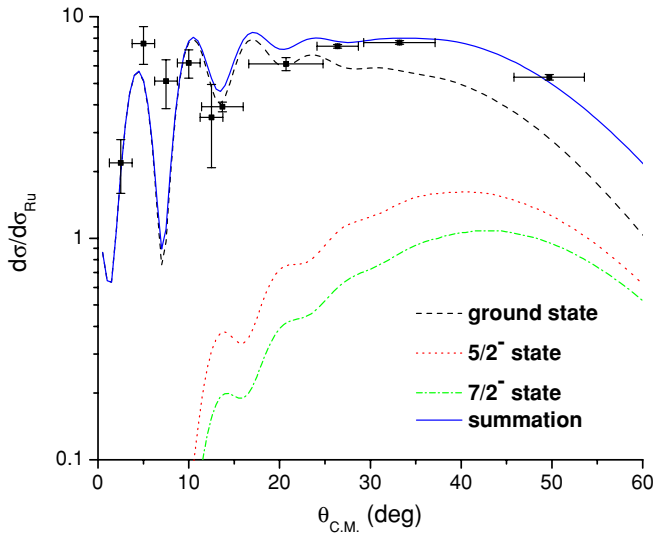

FIG. 8. (Color online) Coupled channel calculation of the differential cross sections for elastic and inelastic scattering of a 25 MeV/nucleon ^{6}He from various states of ^{9}Be target. The sum is compared to the experimental data presented by the solid points.

that the elastic cross section decreases owing to the coupling with the inelastic channels and the sum total of the cross sections for the ground state and the two excited states of ^{9}Be is just somewhat higher than that indicated by the experimental data. We increased the depth of the imaginary potential from 36.4 MeV to 37.0 MeV (set C in Table II) to obtain as good a fit to the data as that presented by the solid line in Fig. 7. As shown in Fig. 8 the inelastic cross sections for the states $5/2^-$ and $7/2^-$ are negligible for c.m. angles up to 20° and, compared to the elastic cross sections, they remain small up to the maximum of the detected angular range. Consequently, the influence of inelastic scattering on our measurement is small and the OP parameters obtained in the present analysis are reliable in the context of the choice of the potential form. The same situation occurred when we started from the OP parameter set A.

IV. CONCLUSIONS

We have measured the differential cross sections of quasielastic scattering of ^{6}He at 25 MeV/nucleon from a ^{9}Be target. A 0° position-sensitive telescope has been used to detect the scattering at very small angles. The alignment has been based on the online measurement of the beam profiles by a set of PPACs and a PSD. The double-folding model has been applied to generate the real part of the OP. An OM analysis has been performed by using the code ECIS97 and various parameters have been studied by the optimal-fit approach to the experimental data. The effect of unstable nuclei relevant to the obtained OP parameters has been discussed. The influence of inelastic scattering has been analyzed by the coupled-channel calculation in the framework of the symmetric rotational model. It has been found that the inelastic cross sections are relatively small over the entire angular range

of our experimental data. Consequently, the obtained optical potential parameters are reliable in the context of the choice of the potential form. Additional experiments performed with a better angular resolution and larger angular range will be useful for studying details of the OP, such as spin-orbit potential and dynamic polarization potential. Further theoretical analysis taking into account the coupling to the continuum (breakup) states of ^{6}He is also strongly encouraged.

ACKNOWLEDGMENTS

This work was supported by the Major State Basic Research Developing Program under Grant No. G2000077403 and the National Natural Science Foundation of China. The authors acknowledge the staffs of the Ring Cyclotron in RIKEN who provided the high-quality ^{13}C primary beam and the staff of the RIBS-Lab for their hospitality and technical support.

[1] M. E. Brandan and G. R. Satchler, Phys. Rep. **285**, 143 (1997).
[2] I. J. Thompson, Nucl. Phys. **A701**, 7c (2002).
[3] G. R. Satchler, *Introduction to Nuclear Reactions*, 2nd ed. (Oxford University Press, New York, 1990).
[4] I. Tanihata *et al*., Phys. Rev. Lett. **55**, 2676 (1985); Phys. Lett. **B206**, 592 (1988).
[5] I. Tanihata, Nucl. Phys. **A685**, 80c (2001).
[6] V. Lapoux *et al*., Phys. Rev. C **66**, 034608 (2002).
[7] B. M. Sherrill, Nucl. Phys. **A685**, 134c (2001).
[8] A. A. Korsheninnikov *et al*., Nucl. Phys. **A617**, 45 (1997).
[9] M. Cortina-Gil *et al*., Phys. Lett. **B401**, 9 (1997).
[10] V. Lapoux *et al*., Phys. Lett. **B517** 18 (2001).
[11] R. Wolski *et al*., Phys. Lett. **B467**, 8 (1999).
[12] G. D. Alkhazov *et al*., Phys. Rev. Lett. **78**, 2313 (1997).
[13] K. Rusek *et al*., Phys. Rev. C **61** 034608 (2000).
[14] T. Kubo *et al*., Nucl. Instrum. Methods B **70**, 309 (1992).
[15] T. Chen, *et al*., High Energy Phys. Nucl. Phys. **27**, 72 (2003).
[16] H. Kumagai, *et al*., Nucl. Instrum. Methods A **470**, 562 (2001); Y. Ye, *et al*., Nucl. Instrum. Methods A **515**, 718 (2003).
[17] M. Zahar *et al*., Phys. Rev. C **49** 1540 (1994).
[18] J. J. Kolata *et al*., Phys. Rev. Lett. **69**, 2631 (1992).
[19] G. R. Satchler and W. G. Love, Phys. Rep. **55**, 183 (1979).
[20] J. Cook, Comput. Phys. Commun. **25**, 125 (1982).
[21] V. Hnizdo *et al*., Phys. Rev. C **24**, 1495 (1981).
[22] A. A. Korsheninnikov *et al*., Nucl. Phys. **A617**, 45 (1997).
[23] L. V. Chulkov *et al*., Europhys. Lett. **8**, 245 (1989).
[24] J. Raynal, coupled-channel code ECIS97 (unpublished).
[25] M. Zahar *et al*., Phys. Rev. C **54**, 1262 (1996).
[26] S. Kox *et al*., Phys. Rev. C **35**, 1678 (1987).
[27] S. Roy *et al*., Phys. Rev. C **52**, 1524 (1995).